

Modeling and simulation in supersonic three-temperature carbon dioxide turbulent channel flow

Guiyu Cao^{a,b}, Yipeng Shi^{c,*}, Kun Xu^d, Shiyi Chen^{a,b,*}

^a*Academy for Advanced Interdisciplinary Studies, Southern University of Science and Technology, Shenzhen, Guangdong 518055, People's Republic of China*

^b*Guangdong-Hong Kong-Macao Joint Laboratory for Data-Driven Fluid Mechanics and Engineering Applications, Southern University of Science and Technology, Shenzhen, Guangdong 518055, People's Republic of China*

^c*Department of Aeronautics & Astronautics Engineering, Peking University, Beijing 100871, People's Republic of China*

^d*Department of Mathematics, Hong Kong University of Science and Technology, Clear Water Bay, Kowloon, Hong Kong*

Abstract

This paper pioneers the direct numerical simulation (DNS) and physical analysis in supersonic three-temperature carbon dioxide (CO_2) turbulent channel flow. CO_2 is a linear and symmetric triatomic molecular, with the thermal non-equilibrium three-temperature effects arising from the interactions among translational, rotational and vibrational modes under room temperature. Thus, the rotational and vibrational modes of CO_2 are addressed. Thermal non-equilibrium effect of CO_2 has been modeled in an extended three-temperature BGK-type model, with the calibrated translational, rotational and vibrational relaxation time. To solve the extended BGK-type equation accurately and robustly, non-equilibrium high-accuracy gas-kinetic scheme is proposed within the well-established two-stage fourth-order framework. Compared with the one-temperature supersonic turbulent channel flow, supersonic three-temperature CO_2 turbulence enlarges the ensemble heat transfer of the wall by approximate 20%, and slightly decreases the ensemble frictional force. The ensemble density and temperature fields are greatly affected, and there is little change in Van Driest transformation of streamwise velocity. The thermal non-equilibrium three-temperature effects of CO_2 also suppress the peak of normalized root-mean-square of density and temperature, normalized turbulent intensities and Reynolds stress. The vibrational modes of CO_2 behave quite differently with rotational and translational modes. Compared with the vibrational temperature fields, the rotational temperature fields have the higher similarity with translational temperature fields, especially in temperature amplitude. Current thermal non-equilibrium models, high-accuracy DNS and physical analysis in supersonic CO_2 turbulent flow can act as the benchmark for the long-term applicability of compressible CO_2 turbulence.

Keywords: Carbon dioxide flow, Vibrational modes, Three-temperature effects, Supersonic turbulent channel flows

1. Introduction

Mars exploration programs are currently experiencing a revival, such as amazing Mars robotic helicopter "Ingenuity" operating on Mars [1]. Mars's atmosphere consists of 95.32% carbon dioxide (CO_2). For accurate predictions of surface drag and heat flux on Martian vehicles, it is necessary to take the peculiarities of CO_2 into account. Different with the dominant diatomic gases nitrogen (N_2) and oxygen (O_2) on earth, CO_2 is a linear and symmetric triatomic molecular, which has three vibrational modes [2]. Triatomic molecular CO_2 is equipped with the inherent thermal non-equilibrium multi-temperature effects arising from the interactions among the translational, rotational and vibrational modes [3, 4].

Carbon dioxide is widely studied in the applications of physical chemistry and fluid dynamics, i.e., CO_2 - N_2 gas laser system [5], environmental green-house problems [6], and Mars entry vehicles [7, 8, 9]. Complex molecular structure and multiple internal energy relaxation mechanisms in CO_2 significantly affect its physical and chemical properties [10]. In fluids community, of special interest is the evaluation of bulk viscosity in CO_2 . Stokes' viscosity relation does not hold for CO_2 [11], as the bulk viscosity can be thousands of times larger than the shear viscosity. Many research works are engaged in experimental and theoretical studies in the bulk viscosity of CO_2 [12, 13]. Recent experiments [14, 15] show that the vibrational modes contribute dominantly to the bulk viscosity of CO_2 , and the bulk viscosity from rotational modes is only one half of its shear viscosity approximately [15]. Thus, the vibrational modes should be modelled carefully when simulating CO_2 flows. In view of the importance of multiple internal energy modes, the multiple internal energy relaxation mechanisms of CO_2 [3, 4] have been modeled and analyzed, which confirm that equilibrium one-temperature gas flow description is not valid for CO_2 flows even under room temperature (i.e., 300K). To the author's knowledge, the thermal non-equilibrium physical models considering the multi-temperature effects of CO_2 and its applications in turbulent flows are seldom reported. For accurate predictions of CO_2 turbulence, it is necessary to take the three-temperature effects of CO_2 into account.

In the past few decades, the gas-kinetic scheme (GKS) based on the Bhatnagar-Gross-Krook (BGK) model [16, 17] has been developed systematically for the computations from low speed flows to hypersonic ones [18, 19]. Based on the time-dependent flux solver, including generalized Riemann problem solver and GKS [20, 21], a reliable two-stage fourth-order framework was provided for developing the high-order GKS (HGKS) into fourth-order accuracy. With the advantage of finite volume GKS and HGKS, they have been naturally implemented as a direct numerical simulation (DNS) tool in simulating turbulent flows [22, 23, 24], especially for compressible turbulence [25, 26]. Aiming to conduct the large-scale DNS, a parallel in-house computational platform of HGKS has been developed in uniform grids and curvilinear grids [27, 28], with high efficiency, fourth-order accuracy and super robustness. In addition, with the discretization of particle velocity space, a unified gas-kinetic

*Corresponding author

Email addresses: caogy@sustech.edu.cn (Guiyu Cao), syp@mech.pku.edu.cn (Yipeng Shi), makxu@ust.hk (Kun Xu), chensy@sustc.edu.cn (Shiyi Chen)

scheme (UGKS) [29, 30] and unified gas-kinetic wave particle method (UGKWP) [31, 32, 33] have been developed for multi-scale physical transport problems. The well-developed HGKS and multi-scale UGKS/UGKWP provides the solid foundation for thermal non-equilibrium multi-temperature modeling and simulation in CO_2 flows. The multi-scale modeling and numerical framework can be applied in multi-scale CO_2 flows, i.e., the Mar's re-entry vehicles from rarefied to continuum regimes. As a starter, current study focuses on the supersonic CO_2 turbulence in the continuum regime.

In this paper, the vibrational modes of CO_2 are addressed, and the translational, rotational and vibrational relaxation time of CO_2 are calibrated. The three-temperature effects of CO_2 are modeled in an extended three-temperature BGK-type model within the well-established kinetic framework [34, 35, 36]. To achieve high-order accuracy in space and time for simulating the supersonic CO_2 turbulence, the non-equilibrium high-accuracy GKS has been constructed with the second-order kinetic flux, fifth-order WENO-Z reconstruction [37], and two-stage fourth-order time discretization [21]. One-temperature supersonic turbulent channel flow [38, 39] is simulated firstly to validate the numerical set-up with bulk Mach number $Ma = 3$ and bulk Reynolds number $Re = 4880$. Considering the translational, rotational, and vibrational specific heats at constant volume, one-temperature supersonic turbulent channel flow of thermally perfect gas has been studied [40]. With implementing the non-equilibrium high-accuracy GKS in the large-scale parallel in-house platform [27, 28], for the first time, the DNS in supersonic three-temperature CO_2 turbulent channel flow is conducted. Compared with the one-temperature supersonic turbulent channel flow, the three-temperature effects of CO_2 are analyzed. Numerical simulation confirms the thermal non-equilibrium three-temperature performance of CO_2 . Both the maximum ensemble temperature and normalized r.m.s. temperature sort from high to low is translational temperature, rotational temperature, and vibrational temperature. Compared with the vibrational temperature fields, the rotational temperature fields has the higher similarity with translational temperature fields both in temperature amplitude and its structure.

For physical modeling and numerical simulation in supersonic three-temperature CO_2 turbulent channel flow, this paper is organized as follows. Section 2 addresses the internal energy modes of CO_2 . Extended thermal non-equilibrium three-temperature BGK-type model and corresponding non-equilibrium high-accuracy GKS for CO_2 are included in Section 3. Numerical examples and discussions are presented in Section 4. The last section is the conclusion and remarks.

2. Internal energy modes of carbon dioxide

Thermal non-equilibrium three-temperature effects of CO_2 mainly arise from the interactions among internal energy modes [4]. This section addresses the vibrational modes of CO_2 , and focuses on the translational, rotational and vibrational relaxation time for the extended three-temperature BGK-type model.

2.1. Rotational and vibrational modes

Carbon dioxide is a linear and symmetric triatomic molecular, with rotational and vibrational internal energy modes. The characteristic rotational temperature is defined as

$\theta_r = h_P^2/(8\pi^2k_B I)$, where h_P is the Planck constant, k_B the Boltzmann constant, I the molecular moment of inertia. For carbon dioxide, $\theta_r = 0.56K$ can be obtained [2], while the θ_r for N_2 and O_2 is $2.88K$ and $2.08K$, respectively. Under room temperature, it is well known that the rotational degrees of freedom (d.o.f.) are assumed to be excited completely for N_2 and O_2 . Since CO_2 is with the smaller characteristic rotational temperature, the rotational d.o.f. of CO_2 are regarded as complete excitation in current study (i.e., CO_2 gas temperature above $300K$).

Carbon dioxide is equipped with three vibrational modes as one symmetric stretching mode ν_1 , one double degenerated bending mode ν_2 , and one asymmetric stretching mode ν_3 . The characteristic vibrational temperature reads $\theta_v = h_P \tilde{\nu} c_L / k_B$, where $\tilde{\nu}$ is the characteristic wavenumber, and c_L the speed of light in the vacuum. In experimental studies of CO_2 , infrared spectrum gives the wavelength for corresponding vibrational modes ν_2 and ν_3 , and Raman spectroscopy provides the wavelength for ν_1 [2]. Table 1 presents the characteristic wavenumber, wavelength ($\lambda = 1/\tilde{\nu}$), characteristic vibrational temperature and corresponding degeneracy of CO_2 . The double degenerated bending modes ν_2 are most likely to be activated with characteristic vibrational temperature $\theta_v = 959.66K$, which is much lower than that of N_2 with $\theta_v = 3521K$ and O_2 with $\theta_v = 2256K$. Thus, the vibrational modes of N_2 and O_2 is usually considered in high-temperature applications, i.e., re-entry vehicles experiencing the temperature above $800K$ [41]. However, the excitation of vibrational modes of CO_2 requires to be modeled and simulated even under the room temperature [4, 15].

| Vibrational mode | Wavenumber($\tilde{\nu}$)/ cm^{-1} | Wavelength(λ)/ μm | θ_v/K | Degeneracy |
|------------------|--|----------------------------------|--------------|------------|
| ν_1 | 1388 | 7.20 | 1997.02 | 1 |
| ν_2 | 667 | 14.99 | 959.66 | 2 |
| ν_3 | 2349 | 4.26 | 3379.69 | 1 |

Table 1: Parameters for three vibrational modes of CO_2 .

With the assumption that there is a unique vibrational temperature at each point in the flow fields, the translational internal energy E_t , rotational internal energy E_r , and vibrational internal energy E_v per unit mass of CO_2 read

$$E_t = \frac{N_t}{2} RT_t, \quad (1)$$

$$E_r = \frac{N_r}{2} RT_r, \quad (2)$$

$$E_v = R \sum_{i=1}^3 g_i \frac{\theta_{v,i}}{e^{\theta_{v,i}/T_v} - 1}, \quad (3)$$

with translational d.o.f. as N_t , rotational d.o.f. as N_r , and vibrational d.o.f. as N_v , where T_t , T_r and T_v represent translational temperature, rotational temperature and vibrational temperature, respectively. In Eq.(3), $\theta_{v,i}$ is the characteristic vibrational temperature of vibrational mode ν_i , and g_i is the corresponding degeneracy of mode ν_i as shown in Table

1. The total specific heat at constant volume C_V can be obtained by the sum of three components as

$$C_V = C_{V,t} + C_{V,r} + C_{V,v}, \quad (4)$$

with

$$C_{V,t} = \frac{N_t}{2} R, \quad (5)$$

$$C_{V,r} = \frac{N_r}{2} R, \quad (6)$$

$$C_{V,v} = \sum_{i=1}^3 g_i \frac{(\theta_{v,i}/T_v)^2}{e^{\theta_{v,i}/T_v} + e^{-\theta_{v,i}/T_v} - 2} R, \quad (7)$$

where $C_{V,t}$, $C_{V,r}$ and $C_{V,v}$ denotes the componential specific heat at constant volume for translational internal energy, rotational internal energy and vibrational internal energy, respectively. In current study, the supersonic CO_2 turbulence is considered above $300K$, thus, translational d.o.f. as $N_t = 3$ and rotational d.o.f. as $N_r = 2$ are adopted. Vibrational d.o.f. as N_v can be obtained by the definition as $C_{V,v} = N_v R/2$, and the specific heat ratio γ is the function of vibrational d.o.f. as

$$N_v = 2 \sum_{i=1}^3 g_i \frac{(\theta_{v,i}/T_v)^2}{e^{\theta_{v,i}/T_v} + e^{-\theta_{v,i}/T_v} - 2}, \quad (8)$$

$$\gamma = \frac{C_P}{C_V} = 1 + \frac{2}{5 + N_v}. \quad (9)$$

In Eq.(9), C_P is the total specific heat at constant pressure. In the high-temperature limit, note that the vibrational d.o.f. as N_v approaches to classical definition with $2 \sum_{i=1}^3 g_i \frac{\theta_{v,i}/T_v}{e^{\theta_{v,i}/T_v} - 1}$.

For compressible wall-bounded turbulence, the Prandtl number Pr plays a key role in determining the statistical turbulent quantities [27], especially for density and temperature fields. For CO_2 , the Pr can be calculated as $Pr = \mu C_P / \kappa$, where shear viscosity μ and thermal conductivity κ depends on the translational temperature T_t as subsequent Eq.(10) and Eq.(12), and C_P relies on the vibrational temperature as Eq.(9). Figure 1 presents the comparisons on γ and Pr between CO_2 and air. For air, the specific heat ratio γ almost keeps as 1.4 up to $800K$, and Pr is fixed at approximate 0.7 between $300K$ and $800K$. In terms of CO_2 , experimental measurements on γ and Pr show the strong temperature-dependent behavior [42]. We find the numerical profile of γ in CO_2 with Eq.(9) agrees well with the experimental one. The numerical profile of Pr is calculated with the assumption of $T_t = T_v$, and this assumption dose not hold for experimental measurement. Thus, it is reasonable to find the discrepancy in Pr between the numerical profile and experimental result. In following simulation, without the assumption of $T_t = T_v$ as shown in Figure 1, the Pr of CO_2 depends on the practical translational and vibrational temperatures. Notice that the γ and Pr must be computed locally in each time step for each computational grid

[34].

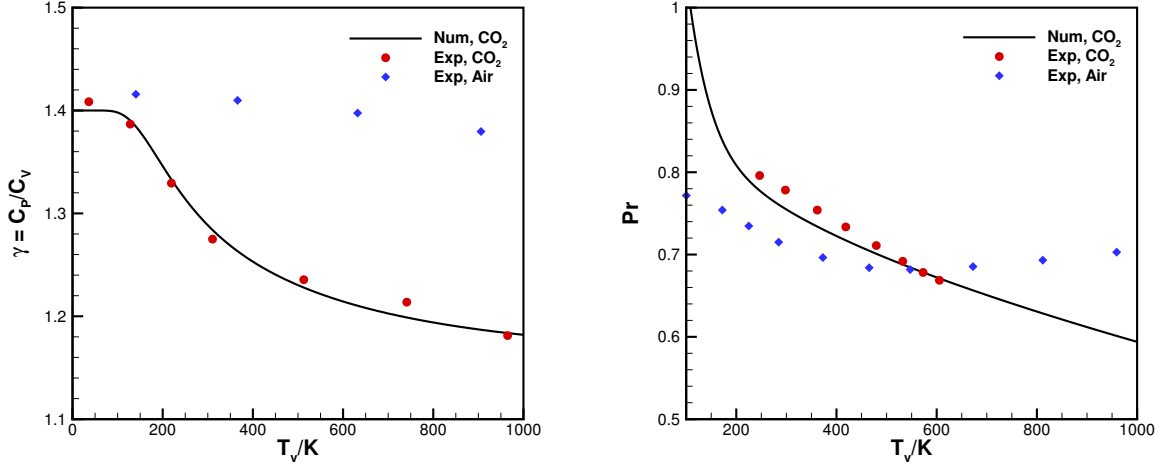


Figure 1: Comparisons on the specific heat ratio γ (left) and Prandtl number Pr (right) for CO_2 and air. The numerical profile of Pr is calculated with the assumption $T_t = T_v$. Experimental results are adapted from the Ref [42].

2.2. Translational, rotational and vibrational relaxation time

For CO_2 gas flows, non-equilibrium translational, rotational, and vibrational internal modes are equipped with different relaxation time. Aiming to the following construction of thermal non-equilibrium three-temperature BGK-type model, the translational, rotational and vibrational relaxation time requires to be determined firstly. Translational relaxation time τ_t is related with shear viscosity μ , and the power law [42] gives the approximation of shear viscosity as

$$\mu(T_t) = \mu_0 \left(\frac{T_t}{T_0} \right)^{n_t}, \quad (10)$$

where T_t is the translational temperature, $n_t = 0.79$ and $\mu_0 = 1.370 \times 10^{-5} kg/(m \cdot s)$ at $T_0 = 273K$ for CO_2 is approximately valid between $209K$ and $1700K$. While, $n_t = 0.666$ and $\mu_0 = 1.716 \times 10^{-5} kg/m \cdot s$ for air is approximately valid between $210K$ and $1900K$. From Chapman-Enskog expansion [17, 19], the translational relaxation time τ_t of CO_2 can be obtained by $\tau_t = \mu/p$, where p is the pressure. Thus, the corresponding power law of translational relaxation time τ_t reads

$$\tau_t = \tau_{t0} \left(\frac{T_t}{T_0} \right)^{n_t}, \quad (11)$$

where $\tau_{t0} = 1.35 \times 10^{-10} s$ at $T_0 = 273K$ with the atmosphere pressure $101.325 \times 10^3 Pa$. The power law also gives the approximation of thermal conductivity κ [42] as

$$\kappa(T_t) = \kappa_0 \left(\frac{T_t}{T_0} \right)^{n_\kappa}, \quad (12)$$

where $n_\kappa = 1.30$ and $\kappa_0 = 1.46 \times 10^{-2} W/(m \cdot K)$ at $T_0 = 273K$ for CO_2 is approximately valid between $180K$ and $700K$. While, $n_\kappa = 0.81$ and $\kappa_0 = 2.41 \times 10^{-2} W/(m \cdot K)$ for air is valid between $210K$ and $2000K$. The thermal conductivity in Eq.(12) gets involved with the calculation of Pr as shown in Figure 1 and following numerical simulation in CO_2 turbulence. For comparison, the Sutherland law for shear viscosity and thermal conductivity of CO_2 and air, as well as the curve-fit expression in the shear viscosity of CO_2 [7] over a much wider range of translational temperature has been provided in Appendix A.

The rotational relaxation time τ_r and vibrational relaxation time τ_v are related with the bulk viscosity η_b [13], which is given by

$$\eta_b = \eta_{b,c} + \eta_{b,int}, \quad (13)$$

where $\eta_{b,c}$ represents the effect of elastic collisions, and $\eta_{b,int}$ accounts for the inelastic collisional contribution of the internal d.o.f. [43]. For dilute gas, $\eta_{b,c}$ can be neglected, resulting in

$$\eta_b \approx \eta_{b,int} = (\gamma - 1)^2 \sum_{i=1}^N \frac{C_{V,i}}{R} p \tau_i, \quad (14)$$

where γ is the specific heat ratio as Eq.(9), R the gas constant, $C_{V,i}$ the specific heat at constant volume as Eq.(5) - Eq.(7), and τ_i the relaxation time for the i th internal energy mode. Assuming that the rotational and vibrational modes relax independently with a single rotational relaxation time τ_r and vibrational relaxation time τ_v , the bulk viscosity as Eq.(14) can be rewritten as

$$\eta_b = \eta_b^r + \eta_b^v, \quad (15)$$

with

$$\eta_b^r = (\gamma - 1)^2 \frac{N_r}{2} p \tau_r, \quad (16)$$

$$\eta_b^v = (\gamma - 1)^2 \frac{C_{V,v}}{R} p \tau_v. \quad (17)$$

η_b^r denotes the componential bulk viscosity arises from the rotational modes, and η_b^v the componential bulk viscosity results from the vibrational modes.

The power law of CO_2 for rotational relaxation time is calibrated by Eq.(16), with the combination of experimental data [15] and Parker equation [44, 45]. As reported in experimental study [15], the vibrational modes remain frozen when measuring the bulk viscosity of CO_2 with Rayleigh-Brillouin light scattering spectroscopy at $532nm$. In such circumstance,

the rotational modes contribute solely to the bulk viscosity, and Eq.(15) reduces to $\eta_b = \eta_b^r$. Thence, the seminal estimated experimental data of η_b^r using Hammond-Wiggings hydrodynamic model [15] is utilized to calibrate the τ_r . Power law of rotational relaxation time τ_r is given by

$$\tau_r = \tau_{r0} \left(\frac{T_t}{T_0} \right)^{n_r}, \quad (18)$$

where $n_r = 1.59$ and $\tau_{r0} = 2.99 \times 10^{-10} s$ at $T_0 = 273K$ is approximately valid between $250K$ and $2000K$ with the atmosphere pressure. The details in calibrating the rotational relaxation time τ_r can be find in Appendix B. With the well-known calibration of $p\tau_v$ [13], the vibrational relaxation time can be calibrated as

$$\tau_v = \tau_{v0} \left(\frac{T_t}{T_0} \right)^{n_v}, \quad (19)$$

where $n_v = -1.353$ and $\tau_{v0} = 1.89 \times 10^{-6} s$ at $T_0 = 800K$ is approximately valid between $300K$ and $1700K$ with the atmosphere pressure.

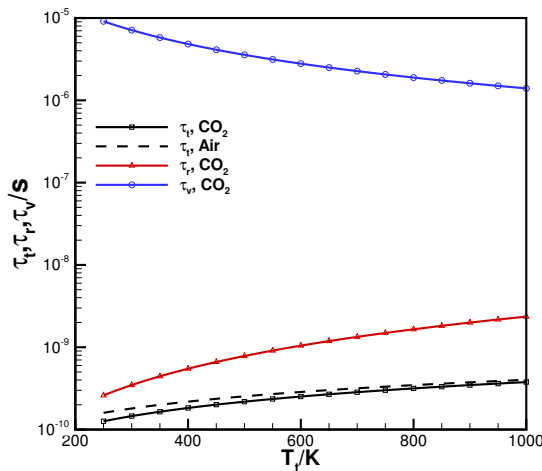


Figure 2: Comparisons on translational relaxation time τ_t , rotational relaxation time τ_r and vibrational relaxation time τ_v for CO_2 and air.

As power laws of Eq.(11), Eq.(18) and Eq.(19) present, all relaxation times only depend on the translational temperature. Figure 2 presents the comparisons on translational, rotational and vibrational relaxation time for CO_2 and air. In Figure 2, the translational relaxation time of air is slightly larger than that of CO_2 . We clearly observe that the vibrational relaxation time τ_v can be approximately thousands of times longer than that of τ_t and τ_r . Current quantitative calibration on τ_t , τ_r and τ_v deviates from the previous theoretical calculations using kinetic theory [10], while the qualitative behaviors are similar. It should be noted that the bulk viscosity of CO_2 is mainly dominated by the η_b^v arising from the vibrational modes [15]. Thus, present τ_v indeed gives the large bulk viscosity with Eq.(17), which is consistent with the findings of inherent large bulk viscosity of CO_2 [11, 43].

3. Three-temperature kinetic model and numerical scheme for carbon dioxide

In this section, an extended thermal non-equilibrium three-temperature BGK-type model for CO_2 is introduced with well-calibrated relaxation time. The three-temperature kinetic equation is going to be solved by the proposed finite-volume non-equilibrium high-accuracy GKS.

3.1. Three-temperature BGK-type model

In terms of one-temperature equilibrium gas flow, the BGK model [16] has been well proposed. For thermal non-equilibrium three-temperature diatomic gas flow, the extended BGK-type model [34, 46] reads

$$\frac{\partial f}{\partial t} + u_i \frac{\partial f}{\partial x_i} = \frac{f^v - f}{\tau_t} + \frac{f^r - f^v}{\tau_r} + \frac{g - f^r}{\tau_v} \equiv \frac{f^v - f}{\tau_t} + Q_v, \quad (20)$$

where $f(\mathbf{x}_{i+1/2, j_m, k_n}, t, \mathbf{u}, \xi_r, \xi_v)$ is the number density of molecules at position $(x_1, x_2, x_3)^T$ and time t , with particle velocity $\mathbf{u} = (u_1, u_2, u_3)^T$ and internal energy $(\xi_r, \xi_v)^T$. The left hand side of Eq.(20) represents the free streaming of molecules in space, and the right side denotes the collision term. In Eq.(20), two intermediate equilibrium states f^v and f^r , and Maxwellian distribution g are introduced with three temperatures T_t , T_r and T_v as

$$f^v = \rho \left(\frac{\lambda_t}{\pi}\right)^{\frac{N_t}{2}} e^{-\lambda_t(u_i - U_i)^2} \left(\frac{\lambda_r}{\pi}\right)^{\frac{N_r}{2}} e^{-\lambda_r \xi_r^2} \left(\frac{\lambda_v}{\pi}\right)^{\frac{N_v}{2}} e^{-\lambda_v \xi_v^2}, \quad (21)$$

$$f^r = \rho \left(\frac{\lambda_t}{\pi}\right)^{\frac{N_t}{2}} e^{-\lambda_t(u_i - U_i)^2} \left(\frac{\lambda_r}{\pi}\right)^{\frac{N_r}{2}} e^{-\lambda_r \xi_r^2}, \quad (22)$$

$$g = \rho \left(\frac{\lambda_t}{\pi}\right)^{\frac{N_t}{2}} e^{-\lambda_t(u_i - U_i)^2}, \quad (23)$$

where ρ is the density, \mathbf{U} denotes three-dimension velocities $(U_1, U_2, U_3)^T$, $\lambda_t = m_0/(2k_B T_t)$ is related to the translational temperature T_t , $\lambda_r = m_0/(2k_B T_r)$ and $\lambda_v = m_0/(2k_B T_v)$ account for the rotational temperature T_r and vibrational temperature T_v , respectively. Above extended BGK-type kinetic model has the similarity with the two relaxation time BGK models for gases with internal d.o.f. [47, 48]. For triatomic molecule CO_2 , we reasonably adopt above three-temperature extend BGK-type model, with the well-calibrated relaxation time as Eq.(11), Eq.(18) and Eq.(19). The right-hand-side collision operator as Eq.(20) contains three terms, corresponding to the elastic collision ($f \rightarrow f^v$) and inelastic collisions ($f^v \rightarrow f^r$ and $f^r \rightarrow g$). As shown in Figure 2, for multiple relaxation process of CO_2 , notice that the inelastic collision takes longer time than that of elastic collision. The additional term Q_v resulting from the inelastic collisions accounts for the internal energy exchange among the translational, rotational and vibrational internal energy.

The relation between density ρ , momentum $\rho \mathbf{U}$, total energy ρE , rotational internal energy ρE_r , and internal vibrational energy ρE_v are determined by taking moments of the

intermediate equilibrium distribution function f^v as

$$\mathbf{Q} \equiv \int \boldsymbol{\psi}_v f^v d\Xi_v = (\rho, \rho\mathbf{U}, \rho E, \rho E_r, \rho E_v)^T, \quad (24)$$

with the vector of extended collision invariants $\boldsymbol{\psi}_v = (1, u_1, u_2, u_3, \frac{1}{2}(u_1^2 + u_2^2 + u_3^2 + \xi_r^2 + \xi_v^2), \frac{1}{2}\xi_r^2, \frac{1}{2}\xi_v^2)^T$ and $d\Xi_v = du_1 du_2 du_3 d\xi_r d\xi_v$. In Eq.(24), total energy is $E = \mathbf{U}^2/2 + E_t + E_r + E_v$. Eq.(20) introduces the new rotational and vibrational temperatures T_r and T_v , thus, the constraints of rotational and vibrational internal energy relaxation have to be imposed on the extended kinetic model to self-consistently determine all unknowns. Since only mass, momentum and total energy are conserved during molecule collisions, the compatibility condition for the collision term turns into

$$\mathbf{S} \equiv \int \left(\frac{f^v - f}{\tau_t} + Q_v \right) \boldsymbol{\psi}_v d\Xi_v = (0, 0, 0, 0, 0, S_r, S_v)^T. \quad (25)$$

Source terms S_r and S_v are from the internal energy exchange among translational, rotational and vibrational modes during inelastic collision. These source terms cannot be derived from the BGK model itself. These two source terms for the rotational internal energy and vibrational internal energy can be modeled through the Landau-Teller-Jeans-type relaxation model [34, 36], which read

$$S_r = \frac{(\rho E_r)^{eq} - \rho E_r}{\tau_r}, \quad (26)$$

$$S_v = \frac{(\rho E_v)^{eq} - \rho E_v}{\tau_v}. \quad (27)$$

For CO_2 , the rotational and vibrational relaxation time τ_r and τ_v have been determined by Eq.(18) and Eq.(19). The left unknown equilibrium rotational internal energy $(\rho E_r)^{eq}$ and vibrational one $(\rho E_v)^{eq}$ are determined by the assumption $T_v = T_r = T_t = T^{eq}$ [34, 36], i.e.,

$$T^{eq} \equiv \frac{N_t T_t + N_r T_r + N_v T_v}{N_t + N_r + N_v}, \quad (28)$$

$$(\rho E_r)^{eq} = \frac{N_r}{2} \rho R T^{eq}, \quad (29)$$

$$(\rho E_v)^{eq} = \frac{N_v}{2} \rho R T^{eq}, \quad (30)$$

with the translational d.o.f. as N_t , rotational d.o.f. as N_r and vibrational d.o.f. as N_v . Up to this point, the thermal non-equilibrium three-temperature BGK-type model for CO_2 is completed with the well-determined relaxation time τ_t , τ_r , and τ_v , as well as the modeling source terms S_r and S_v .

Using the intermediate equilibrium state f^v , with the frozen of rotational and vibrational

internal energy exchange, the 1st-order Chapman-Enskog expansion [17] gives

$$f = f^v - \tau_t \left(\frac{\partial f^v}{\partial t} + u_i \frac{\partial f^v}{\partial x_i} \right), \quad (31)$$

from which the corresponding non-equilibrium three-temperature macroscopic governing equations in three-dimensions can be derived [36]. The technical details in the standard derivation of three-temperature macroscopic equations are similar as that of deriving two-temperature macroscopic equations [49], which are omitted in this paper. The key finding is that two additional equations get involved with above source terms Eq.(26) and Eq.(27), which govern the evolutionary dynamics of rotational internal energy ρE_r and vibrational internal energy ρE_v . Thus current thermal non-equilibrium three-temperature macroscopic system goes beyond the one-temperature supersonic turbulent channel flow of thermally perfect gas [40]. The non-equilibrium three-temperature macroscopic equations give the fixed Prandtl number $Pr = 1$. In the numerical simulation of supersonic CO_2 turbulent channel flow, the heat flux through the cell interface will be corrected to obtain the targeted Pr to any realistic value [42]. The three-temperature BGK-type equation as Eq.(20) is going to be solved by following non-equilibrium high-accuracy GKS, as the numerical fluxes at cell interfaces are evaluated based on the time-dependent gas distribution solution.

3.2. Non-equilibrium high-accuracy gas-kinetic scheme

For finite-volume non-equilibrium GKS, the key procedure is updating the macroscopic flow variables inside each control volume through the numerical fluxes. In this section, the spatial and temporal high-accuracy non-equilibrium GKS is proposed within the two-stage fourth-order framework [21].

Taking moments of the extended three-temperature BGK-type model as Eq.(20) and integrating with respect to control volume, the finite volume scheme can be expressed as

$$\frac{d(\mathbf{Q}_{ijk})}{dt} = -\frac{1}{|\Omega_{ijk}|} \sum_{s=1}^6 \mathbb{F}_s(t) + \mathbf{S}_{ijk}, \quad (32)$$

where \mathbf{Q}_{ijk} is the cell averaged macroscopic variables as Eq.(24), \mathbf{S}_{ijk} is the cell averaged source term as Eq.(25). The control volume $\Omega_{ijk} = [(x_1)_i - \Delta x_1/2, (x_1)_i + \Delta x_1/2] \cdot [(x_2)_j - \Delta x_2/2, (x_2)_j + \Delta x_2/2] \cdot [(x_3)_k - \Delta x_3/2, (x_3)_k + \Delta x_3/2]$, $|\Omega_{ijk}|$ is the volume of Ω_{ijk} and $\mathbb{F}_s(t)$ is the time-dependent numerical flux across the cell interface Σ_s . The numerical flux $\mathbb{F}_s(t)|_{x_1}$ in x_1 - direction is given as example

$$\begin{aligned} \mathbb{F}_s(t)|_{x_1} &= \iint_{\Sigma_s|_{x_1}} \mathbf{F}(\mathbf{Q}) \cdot \mathbf{n} d\sigma \\ &= \sum_{m,n=1}^2 \omega_{mn} \int \psi_v u_1 f(\mathbf{x}_{i+1/2,j_m,k_n}, t, \mathbf{u}, \xi_r, \xi_v) d\xi_v \Delta x_2 \Delta x_3, \end{aligned} \quad (33)$$

where \mathbf{n} is the outer normal direction. The Gaussian quadrature is used over the cell interface

for Eq.(33), where ω_{mn} is the quadrature weight, $\mathbf{x}_{i+1/2,j_m,k_n} = [(x_1)_{i+1/2}, (x_2)_{j_m}, (x_3)_{k_n}]^T$, and $[(x_2)_{j_m}, (x_3)_{k_n}]$ is the quadrature point of cell interface $[(x_2)_j - \Delta x_2/2, (x_2)_j + \Delta x_2/2] \cdot [(x_3)_k - \Delta x_3/2, (x_3)_k + \Delta x_3/2]$. When constructing numerical fluxes for Eq.(20), the secondary relaxation term Q_v is splitly taken into account as the source term \mathbf{S}_{ijk} in Eq.(32).

Without considering Q_v , the gas distribution function $f(\mathbf{x}_{i+1/2,j_m,k_n}, t, \mathbf{u}, \xi_r, \xi_v)$ in the local coordinate can be obtained by the integral solution of Eq.(20) as

$$f(\mathbf{x}_{i+1/2,j_m,k_n}, t, \mathbf{u}, \xi_r, \xi_v) = \frac{1}{\tau_t} \int_0^t f^v(\mathbf{x}', t', \mathbf{u}, \xi_r, \xi_v) e^{-(t-t')/\tau_t} dt' + e^{-t/\tau_t} f_0(-\mathbf{u}t, \xi_r, \xi_v), \quad (34)$$

where $\mathbf{x}' = \mathbf{x}_{i+1/2,j_m,k_n} - \mathbf{u}(t - t')$ is the trajectory of molecule on grids, f_0 the initial gas distribution function, and f^v the corresponding intermediate equilibrium state in the form of Eq.(21). Along the line of GKS [18], for the multi-dimensional kinetic solver, f^v and f_0 can be constructed as

$$f^v = f_0^v(1 + \bar{a}_1 x_1 + \bar{a}_2 x_2 + \bar{a}_3 x_3 + \bar{A}t), \quad (35)$$

and

$$f_0 = \begin{cases} f_l^v[1 + (a_1^l x_1 + a_2^l x_2 + a_3^l x_3) - \tau_t(a_1^l u_1 + a_2^l u_2 + a_3^l u_3 + A_l)], & x \leq 0, \\ f_r^v[1 + (a_1^r x_1 + a_2^r x_2 + a_3^r x_3) - \tau_t(a_1^r u_1 + a_2^r u_2 + a_3^r u_3 + A_r)], & x > 0, \end{cases} \quad (36)$$

where f_l^v and f_r^v are the initial gas distribution functions on both sides of a cell interface Σ_s . f_0^v is the initial intermediate equilibrium state located at the cell interface, which can be determined through the compatibility condition

$$\int \boldsymbol{\psi}_v f_0^v d\Xi = \int_{u_1 > 0} \boldsymbol{\psi}_v f_l^v d\Xi_v + \int_{u_1 < 0} \boldsymbol{\psi}_v f_r^v d\Xi_v. \quad (37)$$

Substituting f^v and f_0 into Eq.(34), the time-dependent gas distribution function at the Gaussian point is evaluated as

$$\begin{aligned} f(\mathbf{x}_{i+1/2,j_m,k_n}, t, \mathbf{u}, \xi_r, \xi_v) &= (1 - e^{-t/\tau_t}) f_0^v + ((t + \tau_t) e^{-t\tau_t} - \tau_t)(\bar{a}_1 u_1 + \bar{a}_2 u_2 + \bar{a}_3 u_3) f_0^v \\ &\quad + (t - \tau_t + \tau_t e^{-t\tau_t}) \bar{A} f_0^v \\ &\quad + e^{-t/\tau_t} f_l^v [1 - (\tau_t + t)(a_1^l u_1 + a_2^l u_2 + a_3^l u_3) - \tau_t A_l] H(u_1) \\ &\quad + e^{-t/\tau_t} f_r^v [1 - (\tau_t + t)(a_1^r u_1 + a_2^r u_2 + a_3^r u_3) - \tau_t A_r] (1 - H(u_1)). \end{aligned} \quad (38)$$

With the relation of macroscopic variables and intermediate equilibrium distribution function f^v , the spatial mesoscopic coefficients $\bar{a}_1, a_1^l, \dots, a_3^l, a_3^r$ and temporal mesoscopic coefficients \bar{A}, A_l, A_r in Eq.(38) can be determined and details are presented in Appendix C. It is noticed that Eq.(38) provides a gas evolution process from kinetic scale to hydrodynamic scale on grids, where both inviscid and viscous fluxes are recovered from a time-dependent and multi-dimensional gas distribution function at a cell interface. This flux function couples the inviscid and all dissipative terms [18, 35], and has advantages in comparison with

traditional hydrodynamic solver in which the Riemann solver [50] and central difference are used for the inviscid and viscous terms splitly. For Prandtl number fix, similar to Ref [18], the total energy flux $\mathbf{F}(\rho E)$ in Eq.(33) is modified as $\mathbf{F}^{new}(\rho E) = \mathbf{F}(\rho E) + (1/Pr - 1)q$, where the time-dependent heat flux through the cell interface can be evaluated precisely by $q = \int(u - U)\{[(u_i - U_i)^2 + \xi_r^2 + \xi_v^2]/2\}fd\Xi_v$. As presented in Section 2.1, Pr depends on both the translational and vibrational temperatures, which is computed locally in each time step for each computational grid.

With the time-dependent kinetic flux as Eq.(38), the second-order accuracy can be achieved by one step integration. To achieve high-order accuracy in space and time, the fifth-order WENO-Z spatial reconstruction [37] and two-stage fourth-order time discretization [20, 21] are implemented. For source term in Eq.(32), the one-step forward Euler method is applied in two-stage updating process to guarantee the robustness. Notice that the T_v and N_v as Eq.(3) and Eq.(8) should be calculated in the center of control volume for source term, as well as at the cell interface when calculating non-equilibrium fluxes in Appendix C. Newton–Raphson method is utilized to compute the T_v at $n + 1$ step. With the initial guess T_v at n step, several iterations are enough to obtain the convergent solution, i.e., with convergence error $\epsilon_{T_v} \equiv ||T_v^* - T_v^{**}||/T_v^n \leq 10^{-8}$ where T_v^* and T_v^{**} are the successive iterated value during the iteration process. $||\phi||$ denotes the absolute value of ϕ . The present non-equilibrium high-accuracy GKS has been constructed with the second-order kinetic flux as Eq.(38), fifth-order WENO-Z reconstruction, two-stage fourth-order time discretization. Current non-equilibrium high-accuracy GKS is well implemented in the in-house parallel computational platform for turbulence simulation [26, 28], and the DNS in supersonic CO_2 turbulent channel flow is presented subsequently.

4. Numerical simulation and discussion

Numerical simulations in supersonic turbulent channel flows with bulk Mach number $Ma = 3.0$ and bulk Reynolds number $Re = 4880$ are implemented in this section. The benchmark as equilibrium one-temperature supersonic turbulent channel flow is validated with HGKS [27, 28] firstly. The supersonic thermal non-equilibrium three-temperature CO_2 turbulent channel flow is simulated with detailed physical analysis.

4.1. One-temperature supersonic turbulent channel flow

The computational studies of supersonic turbulent channel flow [38, 40, 51, 39] have been extensively carried out to study the compressible turbulent boundary layer. One-temperature supersonic turbulent channel flow with bulk Mach number $Ma = 3.0$ and bulk Reynolds number $Re = 4880$ [38, 39] is firstly used to validate the high-accuracy of in-house HGKS solver with non-uniform grids [27]. In the computation, the physical domain is $(x, y, z) \in [0, 4\pi H] \times [-H, H] \times [0, 4\pi H/3]$ and the computational domain takes $(\xi, \eta, \zeta) \in [0, 4\pi H] \times [0, 3\pi H] \times [0, 4\pi H/3]$. The coordinate transformation is given as previous studies [27, 28]. The periodic boundary conditions are used in streamwise X -direction and spanwise Z -directions, and the non-slip and isothermal boundary conditions are utilized in wall-normal Y -direction. In what follows, note that X -, Y - and Z - directions are equivalent

as x_1 -, x_2 - and x_3 - directions in Section 3.2. $(U_1, U_2, U_3)^T$ is re-expressed in $(U, V, W)^T$ for convenient comparisons with refereed studies.

The turbulent channel flow is initiated with uniform density $\rho = 1$, and the initial streamwise velocity $U(y)$ profile is given by the perturbed Poiseuille flow profile $U(y) = 1.5(1 - y^2) + \text{white noise}$, where the white noise is added with 10% amplitude of local streamwise velocity. The spanwise and wall-normal velocity is initiated with white noise. The initial uniform pressure is computed through the corresponding initial bulk Mach number and Reynolds number. The targeted non-dimensional parameters bulk Mach number Ma and bulk Reynolds number Re are defined as $Ma = U_b/c_w$, $Re = \rho_b U_b H / \mu_w$. The bulk velocity U_b and bulk density ρ_b are given by $U_b = \int_{-H}^H U(y) dy$ and $\rho_b = \int_{-H}^H \rho(y) dy$. $H = 1$ is the half height of the channel, μ_w the wall molecule viscosity. $c_w = \sqrt{\gamma R T_w}$ is the wall sound speed, T_w the wall temperature and R the gas constant. T_w is set to 1 in current simulation. In current on-temperature validation case, the shear viscosity μ adopts the exact same power law $\mu(T) \propto T^{0.7}$ [38], where T is the equilibrium temperature. The plus unit Y^+ and plus velocity U^+ are defined as $Y^+ = \rho u_\tau y / \mu$, $U^+ = U / u_\tau$ with the friction velocity $u_\tau = \sqrt{\tau_w / \rho_w}$, the wall shear stress $\tau_w = \mu_w \partial U / \partial y|_w$, and the wall density ρ_w . The friction Mach number Ma_τ and the friction Reynolds number Re_τ are given by $Ma_\tau = u_\tau / c_w$ and $Re_\tau = H / \delta_v$ with $\delta_v = \mu_w / (\rho_w u_\tau)$. The heat flux q_w and the non-dimensional heat flux B_q of the wall are defined as $q_w = -\kappa \partial T / \partial y|_w$, $B_q = q_w / (\rho_w C_P u_\tau T_w)$. In the one-temperature validation, the fixed Prandtl number $Pr = 0.70$ is used as refereed simulation [38], which is close to the Pr of air as shown in Figure 1. These statistical quantities are used to quantitatively validate the performance of HGKS and non-equilibrium high-accuracy GKS subsequently.

| Case | Physical domain | $N_x \times N_y \times N_z$ | $\Delta Y_{min}^+ / Y_{N10}^+$ | ΔX^+ | ΔZ^+ |
|------------------|------------------------------------|-----------------------------|--------------------------------|--------------|--------------|
| Ref ₁ | $4\pi H \times 2H \times 4\pi H/3$ | $144 \times 90 \times 60$ | 0.20/17 | 39 | 24 |
| Ref ₂ | $4\pi H \times 2H \times 4\pi H/3$ | $400 \times 210 \times 320$ | 0.65/- | 14.32 | 5.96 |
| G_1 | $4\pi H \times 2H \times 4\pi H/3$ | $128 \times 128 \times 128$ | 0.52/12.94 | 43.36 | 14.45 |

Table 2: Supersonic one-temperature turbulent channel flow: numerical parameters of current validation case G_1 and the reference simulations [38, 39]. "-" means that the data can not be find in the refereed paper.

In this one-temperature supersonic turbulent channel flow simulation, the details of numerical parameters are given in Table 2. The numerical cases of DNS in refereed paper [38] and [39] are denoted as Ref₁ and Ref₂, and case G_1 is implemented by one-temperature HGKS [28]. The spectral method and high-order difference scheme is used in Ref₁ and Ref₂, respectively. ΔY_{min}^+ is the first grid center space off the wall in the wall-normal direction, and Y_{N10}^+ is the plus unit for the first ten points (grid center) off the wall. ΔX^+ and ΔZ^+ are the equivalent plus unit for uniform streamwise and spanwise grids, respectively. As shown in Table 2, the grid resolution of case G_1 meet the requirement for DNS [38]. The constant moment flux is used to determine the external force [28] in transition and the fully developed turbulence periods. The supersonic turbulent channel flow takes longer time to transit than that of near incompressible turbulent channel flow with $Ma = 0.1$. During the

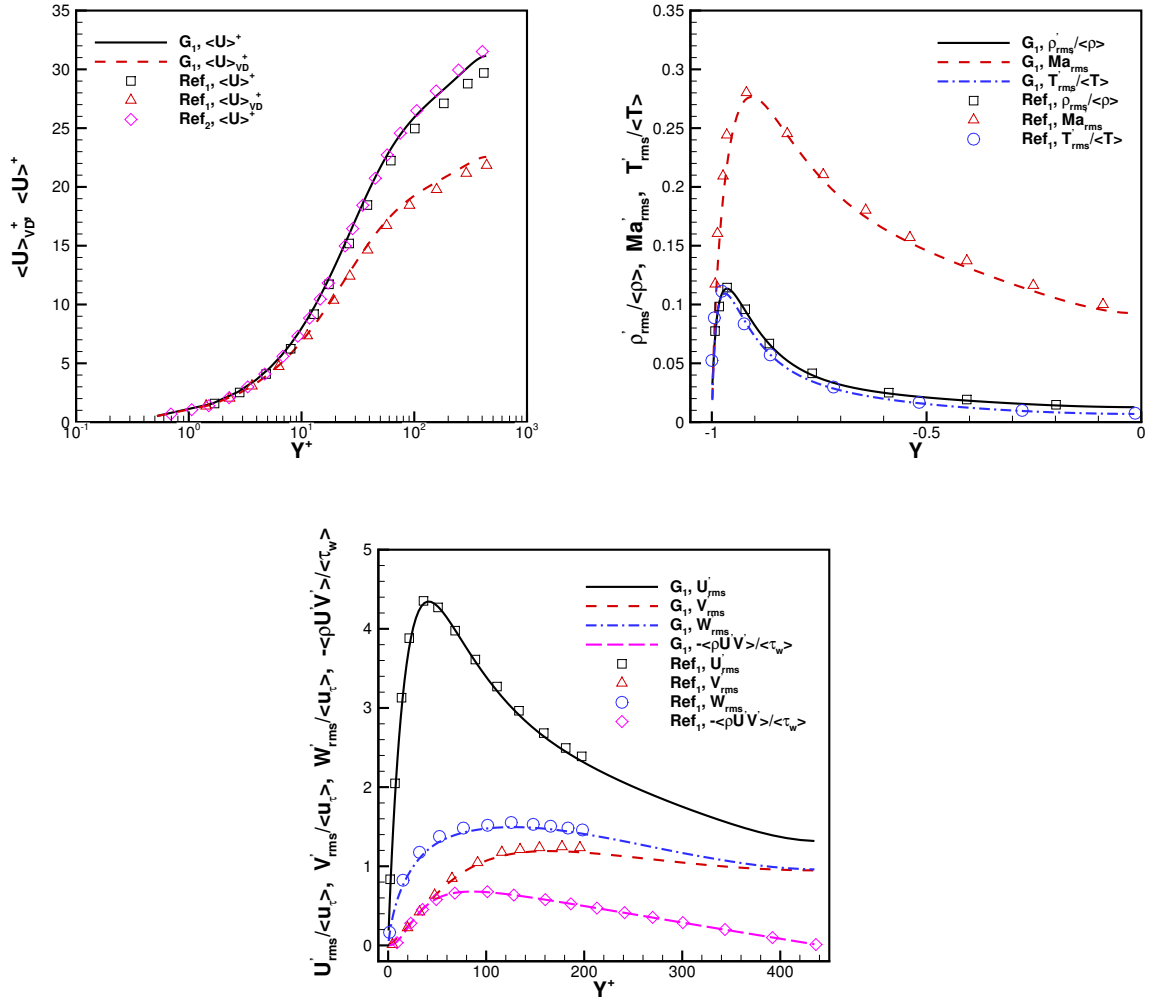


Figure 3: Supersonic one-temperature turbulent channel flow: the profiles of normalized r.m.s. of density $\rho'_{rms}/\langle \rho \rangle$, r.m.s. of Mach number Ma'_{rms} and normalized r.m.s. of temperature $T'_{rms}/\langle T \rangle$ (upper), and the profiles of normalized turbulence intensities $U'_{rms}/\langle u \rangle$, $V'_{rms}/\langle u \rangle$, $W'_{rms}/\langle u \rangle$ and Reynolds stress $-\langle \rho U'V' \rangle/\langle \tau_w \rangle$ (lower).

fully developed turbulence period, 680 characteristic periodic time H/U_b is used to obtain the statistically stationary turbulence. In what follows, the ensemble average of ϕ over time and the X - and Z -directions is represented by $\langle \phi \rangle$. The fluctuation of ϕ is denoted by $\phi' = \phi - \langle \phi \rangle$, and the root-mean square (r.m.s.) of ϕ is defined as $\phi'_{rms} = \sqrt{\langle (\phi - \langle \phi \rangle)^2 \rangle}$, where ϕ represents the density, temperature and velocity, etc. To further quantify the performance of HGKS in one-temperature supersonic turbulent channel flow, the profiles of normalized r.m.s. of density $\rho'_{rms}/\langle \rho \rangle$, r.m.s. of Mach number Ma'_{rms} , and normalized r.m.s. temperature $T'_{rms}/\langle T \rangle$, and the profiles of normalized turbulence intensities (r.m.s. of velocities as $U'_{rms}/\langle u \rangle$, $V'_{rms}/\langle u \rangle$, $W'_{rms}/\langle u \rangle$) and Reynolds stress $-\langle \rho U'V' \rangle/\langle \tau_w \rangle$ are presented in Figure 3. In order to account for the mean property of variations caused by

compressibility, the Van Driest (VD) transformation [52] is proposed for the mean velocity, i.e., density-weighted velocity $\langle U \rangle_{VD}^+ = \int_0^{\langle U \rangle^+} (\langle \rho \rangle / \langle \rho_w \rangle)^{1/2} d\langle U \rangle^+$. Compared with the refereed DNS solution [38], the well-agreed performance of case G_1 confirms the high-accuracy flow-fields has been obtained by current HGKS for one-temperature supersonic turbulent channel flow. The small deviations between the case G_1 and Ref₁ may result from the numerical solutions in different governing equations. For VD transformation of streamwise velocity, the solution from case G_1 matches well with the DNS in very fine grids [39] with fixed Prandtl number $Pr = 0.72$. Subsequently, non-equilibrium high-accuracy GKS for three-temperature model proposed in Section 3.2 is used to simulate supersonic thermal non-equilibrium three-temperature CO_2 turbulent channel flow.

4.2. Three-temperature supersonic CO_2 turbulent channel flow

For the first time, the DNS in supersonic thermal non-equilibrium three-temperature CO_2 turbulent channel flow is implemented. The numerical setup is same as one-temperature validation case G_1 in Section 4.1. The bulk Mach number and bulk Reynolds number take $Ma = 3.0$ and $Re = 4880$. The three-temperature initial flow fields restarts from the one-temperature fully developed turbulence, with initializing three temperatures as $T_t = T_r = T_v$. With absolute wall temperature $T_w = 1$, the equivalent wall temperature $T_{we} = 300K$ is adopted to compute the practical physical temperatures when determining τ_r and τ_v . The isothermal boundary condition is utilized for translational temperature T_t . To the author's knowledge, there is no report on wall boundary condition for CO_2 . In current study, assuming rotational and vibrational modes of CO_2 do not exchange internal energy with the wall, thus, adiabatic boundary condition is used for rotational and vibrational temperatures in wall-normal Y -direction. The realistic wall boundary conditions for rotational and vibrational internal energy of CO_2 deserve to be explored by seminal experimental measurements and theoretical studies.

To balance the wall shear stress, the constant moment flux is used to determine the external force of supersonic thermal non-equilibrium three-temperature CO_2 turbulent channel flow. In Figure 4, note that the mean average of ϕ over whole computational domain (or the two wall planes) is represented by $[\phi]$. After the long running time, the statistical mean variables as $[\rho_w]$, $[\rho E]$, $[\rho E_r]$ and $[\rho E_v]$ in Figure 4 oscillate in a narrow range, indicating that the three-temperature CO_2 turbulent channel flow reaches the fully developed state. Specifically, the mean total energy $[\rho E]$ of one-temperature case G_1 is approximate 94% of current three-temperature CO_2 . The larger mean total energy $[\rho E]$ of three-temperature CO_2 is reasonable, since the CO_2 turbulence is equipped with the additional excited vibrational internal energy. Figure 5 shows three-dimension contours of translational, rotational, and vibrational temperatures of supersonic CO_2 turbulent flows in the fully developed turbulence period. We clearly observe that the contour of vibrational temperature distinguishes from the translational and rotational temperature contours, confirming the thermal non-equilibrium performance.

To quantitatively analyze the three-temperature performance of supersonic CO_2 turbulence, 900 characteristic periodic time H/U_b is used to obtain the statistically stationary three-temperature turbulence. The key ensemble quantities at the wall and the center plane

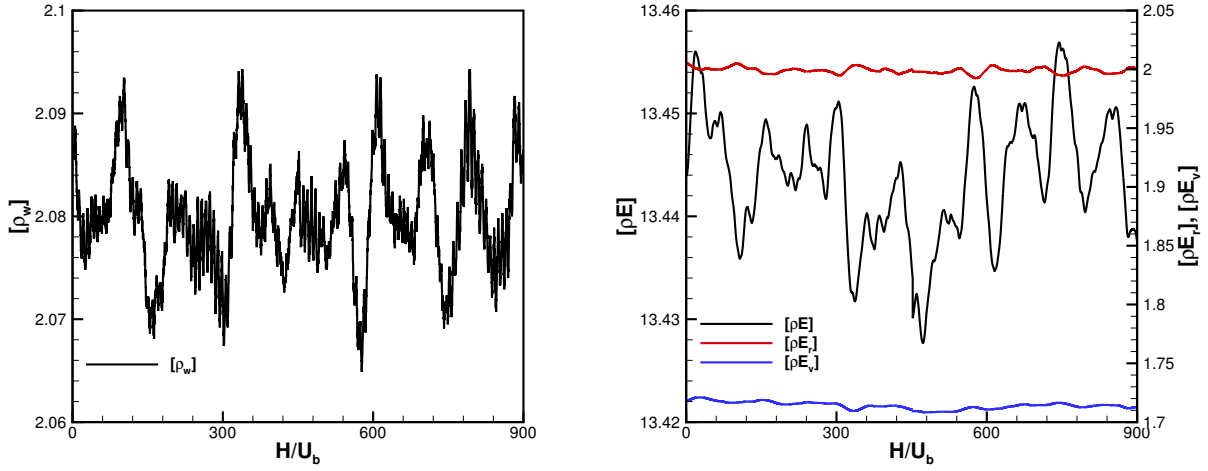


Figure 4: Supersonic thermal non-equilibrium three-temperature CO_2 turbulent channel flow: the time history of mean wall density $[\rho_w]$ (left), and the time history of mean total energy $[\rho E]$, mean rotational internal energy $[\rho E_r]$ and mean vibrational internal energy $[\rho E_v]$ (right).

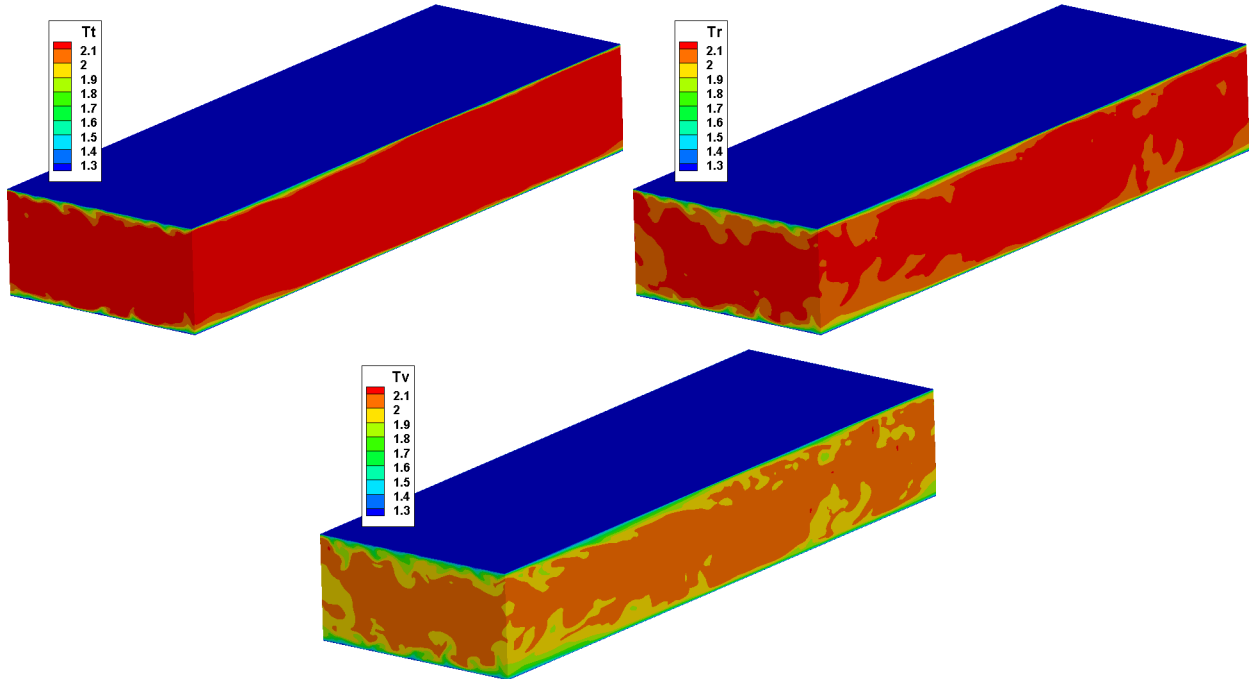


Figure 5: Supersonic thermal non-equilibrium three-temperature CO_2 turbulent channel flow: contours of translational, rotational, and vibrational temperatures.

of channel are presented in Table 3. Running case C_1 denotes the supersonic thermal non-equilibrium three-temperature CO_2 case. Again, ensemble quantities from case G_1 agree well with these of refereed solution in Ref₁ [38]. Compared with the solutions of one-temperature case G_1 , the ensemble friction velocity $\langle u_\tau \rangle$, the ensemble friction Mach number $\langle Ma_\tau \rangle$ and

| Case | $\langle \rho_w \rangle$ | $\langle u_\tau \rangle / U_b$ | $\langle Ma_\tau \rangle$ | $\langle Re_\tau \rangle$ | $\langle B_q \rangle$ | $\langle \rho_c \rangle$ | $\langle T_c^{eq} \rangle$ |
|------------------|--------------------------|--------------------------------|---------------------------|---------------------------|-----------------------|--------------------------|----------------------------|
| Ref ₁ | 2.388 | 0.0387 | 0.116 | 451 | 0.137 | 0.952 | 2.490 |
| G ₁ | 2.407 | 0.0376 | 0.113 | 442 | 0.137 | 0.948 | 2.521 |
| C ₁ | 2.080 | 0.0400 | 0.120 | 406 | 0.127 | 0.966 | 2.084 |

Table 3: Supersonic thermal non-equilibrium three-temperature CO_2 turbulent channel flow: ensemble quantities at the wall and the center plane of channel.

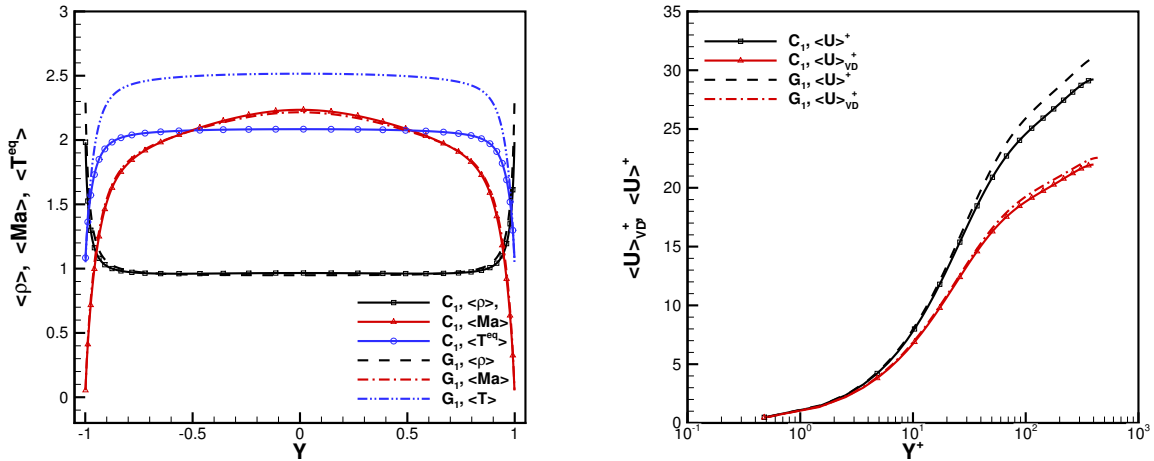


Figure 6: Supersonic thermal non-equilibrium three-temperature CO_2 turbulent channel flow: the profiles of ensemble density $\langle \rho \rangle$, ensemble Mach number $\langle Ma \rangle$, and ensemble equilibrium temperature $\langle T^{eq} \rangle$ (left), and the profiles of ensemble streamwise velocity profiles $\langle U \rangle^+$ and VD transformation of streamwise velocity $\langle U \rangle_{VD}^+$ (right).

the ensemble center density $\langle \rho_c \rangle$ (density at the center plane of channel, namely at $Y = 0$ plane) of case C_1 are slightly larger. The non-dimensional heat flux B_q of the wall of case C_1 is slightly smaller than that of case G_1 . While the ensemble wall density $\langle \rho_w \rangle$, the ensemble friction Reynolds number Re_τ , and the ensemble central equilibrium temperature $\langle T_c^{eq} \rangle$ of case C_1 reduce dramatically. Frictional force and heat transfer of the wall is of special interest in the long-term applicability of compressible CO_2 turbulence. The ensemble frictional force $\langle \tau_w \rangle$ of case G_1 and case C_1 is 3.41×10^{-3} and 3.32×10^{-3} , respectively. While, the ensemble heat flux $\langle q_w \rangle$ of G_1 and C_1 is -0.0309 and -0.0396 , respectively. It is concluded that the thermal non-equilibrium three-temperature effects of CO_2 enlarge the ensemble heat transfer by 20%, and slightly decrease the ensemble frictional force.

For the first-order ensemble statistical quantities in supersonic three-temperature CO_2 turbulent channel flow, the profiles of key ensemble quantities are presented in Figure 6. The equilibrium temperature T^{eq} is defined as Eq.(28). Compared with the one-temperature case G_1 , we observe the large discrepancies in the near-wall density profiles (approximate $\|Y/H\| \geq 0.8$) and the equilibrium temperature profiles in the off-wall region (approximate $\|Y/H\| \leq 0.95$). Both the ensemble wall density and central equilibrium temperature

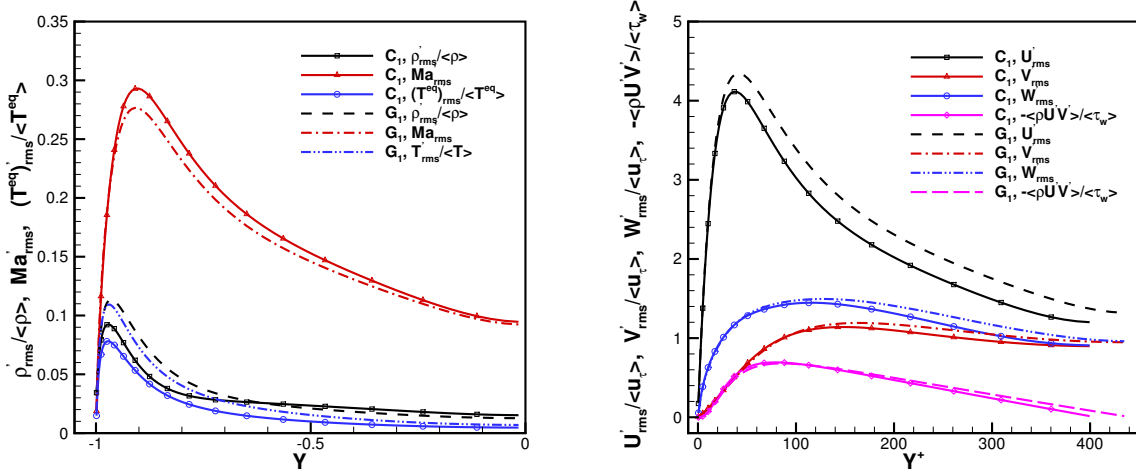


Figure 7: Supersonic thermal non-equilibrium three-temperature CO_2 turbulent channel flow: the profiles of normalized r.m.s. of density $\rho'_{rms}/\langle\rho\rangle$, r.m.s. of Mach number Ma'_{rms} and normalized r.m.s. of equilibrium temperature $(T^{eq})'_{rms}/\langle T^{eq}\rangle$ (left), and the profiles of normalized turbulence intensities $U'_{rms}/\langle u_\tau\rangle$, $V'_{rms}/\langle u_\tau\rangle$, $W'_{rms}/\langle u_\tau\rangle$ and normalized Reynolds stress $-\langle\rho U' V'\rangle/\langle\tau_w\rangle$ (right).

decrease by approximate 15%. It can be concluded that the thermal non-equilibrium three-temperature effects of supersonic CO_2 affect its ensemble thermal quantities greatly. In Figure 6, the ensemble streamwise velocity in the log-law region of case C_1 is lower than that of case G_1 , indicating that the $\langle U \rangle^+$ in log-law region is suppressed by the non-equilibrium three-temperature effects. There is little change in the ensemble Mach number $\langle Ma \rangle$ and ensemble VD transformation of streamwise velocity $\langle U \rangle^+_{VD}$, showing that the VD transformation [52] still works well for supersonic CO_2 turbulent channel flow. Figure 7 shows that the peak normalized r.m.s. of density $\rho'_{rms}/\langle\rho\rangle$ and equilibrium temperature $(T^{eq})'_{rms}/\langle T^{eq}\rangle$ of supersonic three-temperature CO_2 are suppressed near the wall region, and the corresponding peak locations are much closer to the wall than these of case G_1 . While, the peak of r.m.s. of Mach number Ma'_{rms} in case C_1 is larger than that of case G_1 . Compared with one-temperature supersonic turbulent channel flow, Figure 7 shows that the normalized turbulent intensities of three-temperature CO_2 are suppressed above the $Y^+ \approx 20$, $Y^+ \approx 100$, and $Y^+ \approx 40$ regions for $U'_{rms}/\langle u_\tau\rangle$, $V'_{rms}/\langle u_\tau\rangle$, and $W'_{rms}/\langle u_\tau\rangle$, respectively. Correspondingly, the normalized Reynolds stress is suppressed above the $Y^+ \approx 120$ region. In supersonic turbulent channel flow, it can be concluded that the thermal non-equilibrium three-temperature effects of CO_2 suppress the peak of normalized r.m.s. of density and temperature, normalized turbulent intensities and Reynolds stress.

Be of special interest in the non-equilibrium performance of three internal energy modes of supersonic three-temperature CO_2 turbulent channel flow. Figure 8 shows the ensemble average of translational, rotational and vibrational temperatures. At the wall, the three ensemble temperatures sort from the high to low as $\langle T_v \rangle$, $\langle T_r \rangle$, $\langle T_t \rangle$, and the opposite order of three temperatures is observed in the off-wall region (approximate $\|Y/H\| \leq 0.95$). Figure 8 as well shows that the peak of normalized r.m.s. of translational temperature $(T_t)'_{rms}/\langle T_t \rangle$

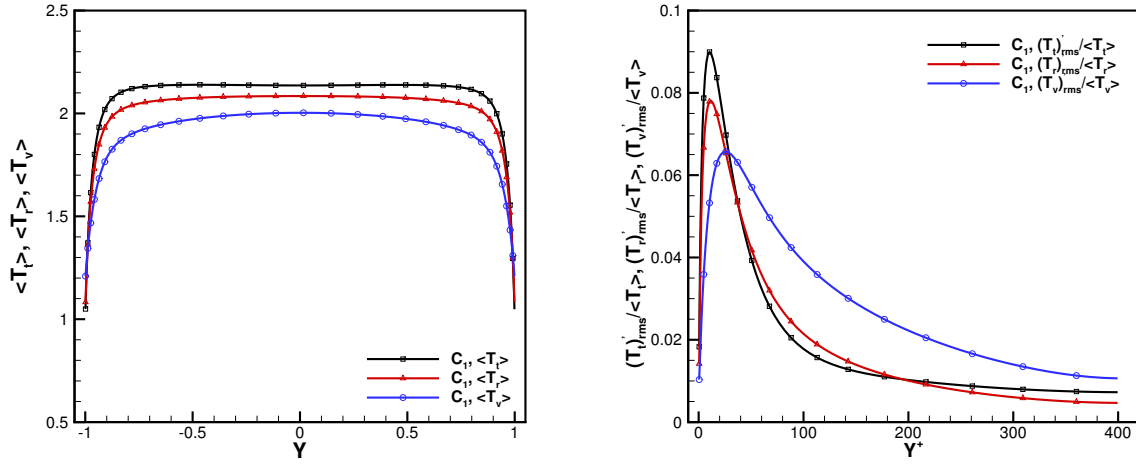


Figure 8: Supersonic thermal non-equilibrium three-temperature CO_2 turbulent channel flow: the ensemble translational, rotational, and vibrational temperature $\langle T_t \rangle$, $\langle T_r \rangle$, $\langle T_v \rangle$ (left), and the normalized r.m.s. of translational, rotational, and vibrational temperature $(T_t)_{rms}'/\langle T_t \rangle$, $(T_r)_{rms}'/\langle T_r \rangle$, $(T_v)_{rms}'/\langle T_v \rangle$ (right).

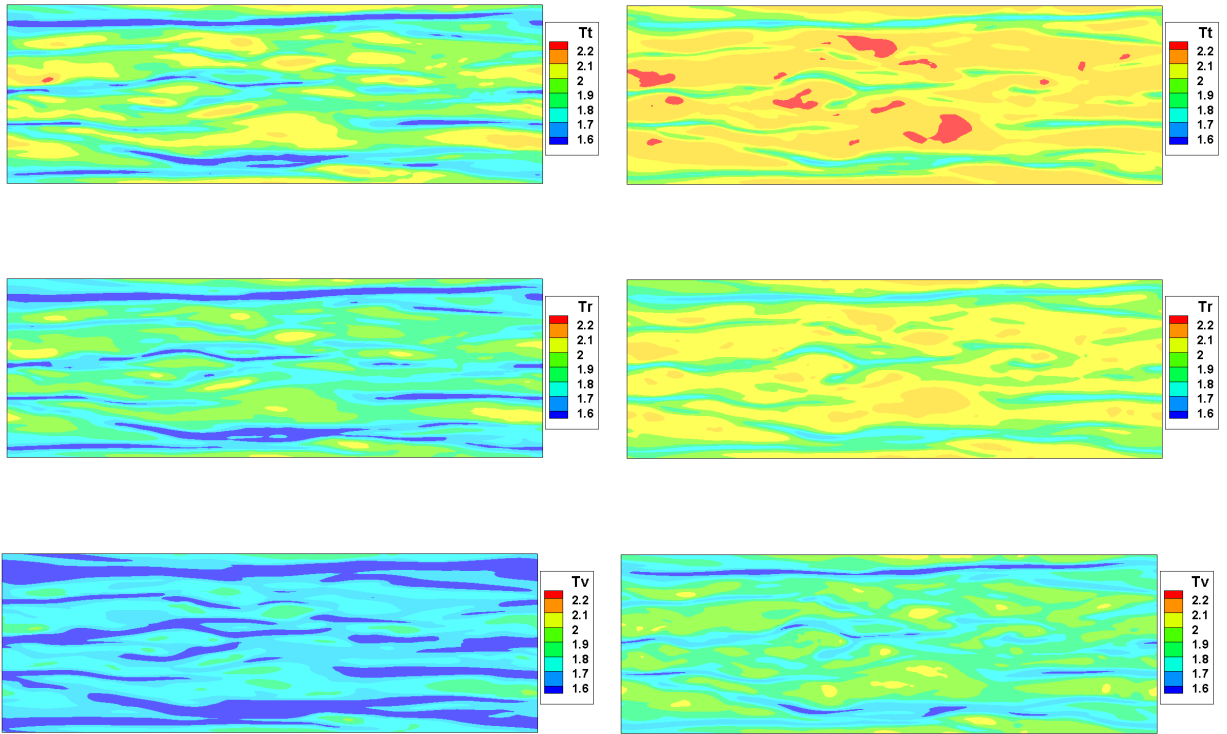


Figure 9: Supersonic thermal non-equilibrium three-temperature CO_2 turbulent channel flow: slices of translational, rotational, and vibrational temperatures at $Y^+ = 20.3$ (left column) and $Y^+ = 40.6$ (right column).

and rotational temperature $(T_r)'_{rms}/\langle T_r \rangle$ is almost co-located at $Y^+ \approx 15$. While the peak location of normalized r.m.s. of vibrational temperature $(T_v)'_{rms}/\langle T_v \rangle$ is far from the wall at $Y^+ \approx 30$. The peak value of normalized r.m.s. of temperatures sorting from the high to low is translational temperature, rotational temperature, and vibrational temperature. Additionally, it is observed that $(T_v)'_{rms}/\langle T_v \rangle$ is larger than $(T_t)'_{rms}/\langle T_t \rangle$ and $(T_r)'_{rms}/\langle T_r \rangle$ above the $Y^+ \approx 30$ region. Figure 9 clearly shows the streamwise low-temperature and high-temperature ribbon-like regions for all three temperatures. At $Y^+ = 20.3$, the low-temperature ribbon-like regions are dominated in vibrational temperature fields, while the high-temperature ones dominate the translational temperature fields at $Y^+ = 40.6$. Compared with the vibrational temperature fields, Figure 9 obviously shows the rotational temperature fields have the higher similarity with translational temperature fields in temperature amplitude. As shown in Figure 2, for CO_2 , the rotational relaxation time τ_r is much closer with the translational relaxation time τ_t . However, the vibrational relaxation time τ_v is thousands of times larger than that of τ_t . Thus, the T_t and T_r are more likely to be equilibrium through the interaction between translational and rotational modes with closer relaxation time. Meanwhile, the much longer relaxation process of vibrational modes may account for its small correlation with translational modes and rotational modes.

5. Conclusion and remarks

The present paper focuses on thermal non-equilibrium three-temperature effects of carbon dioxide (CO_2) in supersonic turbulent channel flow. Essential ingredient has been addressed for compressible CO_2 turbulent flows, namely, the thermal non-equilibrium interactions among translational, rotational, and vibrational modes. The three vibrational modes of CO_2 are addressed, and the double degenerated bending modes ν_2 is equipped with the characteristic vibrational temperature $\theta_v = 959.66K$, which is much lower than that of N_2 and O_2 . Thus, the excitation of vibrational modes of CO_2 requires to be modeled and simulated carefully even under the room temperature. The translational, rotational and vibrational relaxation time of CO_2 are calibrated. Then, CO_2 is modeled in an extended three-temperature BGK-type model within the well-established kinetic framework. To achieve high-order accuracy in space and time for simulating CO_2 turbulence, the non-equilibrium high-accuracy GKS has been constructed with the second-order kinetic flux, fifth-order WENO-Z reconstruction, and two-stage fourth-order time discretization.

With implementing the non-equilibrium high-accuracy GKS in the large-scale parallel in-house solver, the DNS of supersonic CO_2 turbulent channel flow is conducted. Compared with the one-temperature supersonic turbulent channel flow, the three-temperature effects of CO_2 are analyzed. The ensemble frictional force and ensemble heat flux of the wall, as well as the typical ensemble and fluctuating turbulent quantities of supersonic CO_2 turbulent channel flow are investigated. Thermal non-equilibrium three-temperature effects of CO_2 enlarges the ensemble heat transfer of the wall by approximate 20%, and slightly decreases the ensemble frictional force. The ensemble density and temperature fields are greatly affected, and both the ensemble wall density and central equilibrium temperature decrease by approximate 15%. The ensemble streamwise velocity in log-law region is suppressed.

There is little change in VD transformation of streamwise velocity, which shows that the VD transformation still works well for supersonic CO_2 turbulent channel flow. We observe that the peak of normalized r.m.s. of density and temperature, normalized turbulent intensities and Reynolds stress are suppressed in supersonic three-temperature CO_2 turbulent flow.

Numerical simulation confirms the thermal non-equilibrium three-temperature performance of CO_2 . The streamwise low-temperature and high-temperature ribbon-like regions are clearly observed for all three temperatures near the wall region. The vibrational modes of CO_2 behave quite differently with rotational and translational modes. The peak positions of normalized r.m.s. of translational temperature and rotational temperature are almost co-located. Both the maximum ensemble temperature and normalized r.m.s. temperature sort from high to low is translational temperature, rotational temperature, and vibrational temperature. Compared with the vibrational temperature fields, the rotational temperature fields have the higher similarity with translational temperature fields both in temperature amplitude and its structure. The much longer relaxation process of vibrational modes of CO_2 may account for its small correlation with translational modes and rotational modes.

In the future, we expect to explore the interdisciplinary studies on CO_2 transition in supersonic/hypersonic flat plate, i.e., the overheating phenomenon at the late transitional period [53]. The multi-scale numerical framework UGKS and UGKWP [29, 54] also provide the solid foundation in further multi-scale CO_2 flows, i.e., the Mars re-entry vehicles from rarefied to continuum regimes. In addition, the realistic wall boundary conditions for rotational and vibrational internal energy of CO_2 deserve to be explored for more delicate simulations in wall-bounded CO_2 turbulence.

Acknowledgement

Many thanks to Dr. Zhao Wang for helpful discussions on the wall boundary conditions of CO_2 gas flows. This research is supported by the National Numerical Windtunnel project, the Department of Science and Technology of Guangdong Province (2020B1212030001). The authors would like to acknowledge TaiYi supercomputers in the SUSTech for providing high performance computational resources.

Appendix A. Sutherland law and curve-fit shear viscosity of CO_2

For dilute CO_2 gas flows, Sutherland law [42] gives the shear viscosity as

$$\mu(T_t) = \mu_0 \left(\frac{T_t}{T_0}\right)^{\frac{3}{2}} \frac{T_0 + S}{T_t + S}, \quad (39)$$

where the reference shear viscosity $\mu_0 = 1.370 \times 10^{-5} kg/(m \cdot s)$, $T_0 = 273K$ and $S = 222K$ is approximately valid between $190K$ and $1700K$. In terms of air, it is noted that $\mu_0 = 1.716 \times 10^{-5} kg/m \cdot s$, $T_0 = 273K$ and $S = 111K$ for air is approximately valid between $210K$ and $1900K$. Sutherland law gives the thermal conductivity [42] as

$$\kappa(T_t) = \kappa_0 \left(\frac{T_t}{T_0}\right)^{\frac{3}{2}} \frac{T_0 + S}{T_t + S}, \quad (40)$$

where the reference thermal conductivity $\kappa_0 = 1.46 \times 10^{-2}W/(m \cdot K)$, $T_0 = 273K$ and $S = 1800K$ is approximately valid between $180K$ and $700K$. In terms of air, it is noted that $\kappa_0 = 2.41 \times 10^{-2}W/(m \cdot K)$, $T_0 = 273K$ and $S = 194$ is approximately valid between $160K$ and $2000K$.

It is reported that the shear viscosity of CO_2 [7] is well approximated over a wide range of temperature up to $20000K$. The curve-fit expression of shear viscosity reads

$$\mu(T_t) = 0.1exp\{(A \ln T_t + B) \ln T_t + C\}, \quad (41)$$

where $A = -0.01952739$, $B = 1.047818$, and $C = -14.32212$. In Eq.(41), shear viscosity μ is in the unit $kg/(m \cdot s)$.

Appendix B. Calibrated rotational relaxation time of CO_2

This appendix provides the power law for rotational relaxation time τ_r of CO_2 . For bulk viscosity η_b^r arising from the rotational modes, the calibration data of CO_2 [15] is utilized as Table 4. Based on the least-square method, with $T_0 = 273K$, calibration data in Table 4 provides the $\tau_{r0} = 2.99 \times 10^{-10}s$ and $n_r = 4.47$. It should be noted that the data of bulk viscosity in high temperature is not adequate.

| T_t/K | 258.05 | 274.36 | 293.24 | 312.80 | 330.73 | 353.15 |
|----------------|--------|--------|--------|--------|--------|--------|
| η_b^r/μ | 0.226 | 0.180 | 0.188 | 0.198 | 0.200 | 0.191 |

Table 4: Calibration data [15] for determining the rotational relaxation time τ_r of CO_2 .

To absorb the high-temperature information of τ_r , the power n_r should be corrected based on the refereed calculation of CO_2 [45]. The rotational relaxation time is used as $\tau_r = Z_r \tau_t$, where the rotational collision number Z_r is given by Parker equation [44] as

$$Z_r = \frac{Z_r^\infty}{1 + (\pi^{3/2}/2)\sqrt{T^*/T_t} + (\pi + \pi^2/4)(T^*/T_t)}. \quad (42)$$

T^* is the characteristic temperature of inter-molecular potential, and Z_r^∞ is the limiting value. The values $Z_r^\infty = 20.39$ and $T^* = 91.5K$ are used for CO_2 [45]. Thence, with the fixed $T_0 = 273K$ and $\tau_{r0} = 2.99 \times 10^{-10}s$, the $Z_r \tau_t = \tau_{r0}(T/T_0)^{n_r}$ gives the corrected power $n_r = 1.59$ at $T = 2000K$.

Appendix C. Connection between macroscopic variables and mesoscopic coefficients

The connection between the spatial derivatives of macroscopic flow variables and the expansion of intermediate equilibrium distribution function f^v as Eq.(21) reads

$$\frac{\partial Q}{\partial x_i} = \int \frac{\partial f^v}{\partial x_i} \psi_v d\Xi_v \equiv \int a f^v \psi_v d\Xi_v, \quad (43)$$

where a denotes the spatial mesoscopic coefficients in Eq.(38) as

$$a = \mathbf{a}^T \tilde{\boldsymbol{\psi}}_v = a_1 + a_2 u_1 + a_3 u_2 + a_4 u_3 + a_5 (u_1^2 + u_2^2 + u_3^2) + a_6 \xi_r^2 + a_7 \xi_v^2. \quad (44)$$

Eq.(43) can be rewritten into following linear system

$$\frac{1}{\rho} \frac{\partial \mathbf{Q}}{\partial x_i} = \left(\frac{1}{\rho} \int \boldsymbol{\psi}_v \otimes \tilde{\boldsymbol{\psi}}_v^T f^v d\Xi_v \right) \mathbf{a} \equiv \mathbf{M} \mathbf{a}, \quad (45)$$

Each component of $(a_1, \dots, a_6, a_7)^T$ in Eq.(45) can be determined uniquely

$$\begin{cases} a_7 = \frac{4\lambda_v^2}{N_v} B_6, \\ a_6 = \frac{4\lambda_r^2}{N_r} B_5, \\ a_5 = \frac{4\lambda_t^2}{3} (B_4 - U_1 B_1 - U_2 B_2 - U_3 B_3 - B_5 - B_6), \\ a_4 = 2\lambda_t B_3 - 2U_3 a_5, \\ a_3 = 2\lambda_t B_2 - 2U_2 a_5, \\ a_2 = 2\lambda_t B_1 - 2U_1 a_5, \\ a_1 = \frac{1}{\rho} \frac{\partial \rho}{\partial x_i} - U_1 a_2 - U_2 a_3 - U_3 a_4 - (U_1^2 + U_2^2 + U_3^2 + \frac{3}{2\lambda_t}) a_5 - \frac{N_r}{2\lambda_r} a_6 - \frac{N_v}{2\lambda_v} a_7, \end{cases} \quad (46)$$

with

$$\begin{cases} B_1 = \frac{1}{\rho} \left[\frac{\partial(\rho U_1)}{\partial x_i} - U_1 \frac{\partial \rho}{\partial x_i} \right], \\ B_2 = \frac{1}{\rho} \left[\frac{\partial(\rho U_2)}{\partial x_i} - U_2 \frac{\partial \rho}{\partial x_i} \right], \\ B_3 = \frac{1}{\rho} \left[\frac{\partial(\rho U_3)}{\partial x_i} - U_3 \frac{\partial \rho}{\partial x_i} \right], \\ B_4 = \frac{1}{\rho} \left[\frac{\partial(\rho E)}{\partial x_i} - E \frac{\partial \rho}{\partial x_i} \right], \\ B_5 = \frac{1}{\rho} \left[\frac{\partial(\rho E_r)}{\partial x_i} - E_r \frac{\partial \rho}{\partial x_i} \right], \\ B_6 = \frac{1}{\rho} \left[\frac{\partial(\rho E_v)}{\partial x_i} - E_v \frac{\partial \rho}{\partial x_i} \right]. \end{cases} \quad (47)$$

For the temporal mesoscopic coefficient in Eq.(38), the relation between temporal derivatives of macroscopic variables and f^v can be written as

$$\frac{\partial \mathbf{Q}}{\partial t} = \int \frac{\partial f^v}{\partial t} \boldsymbol{\psi}_v d\Xi_v \equiv \int A f^v \boldsymbol{\psi}_v d\Xi_v, \quad (48)$$

with

$$A = \mathbf{A}^T \tilde{\boldsymbol{\psi}}_v = A_1 + A_2 u_1 + A_3 u_2 + A_4 u_3 + A_5 (u_1^2 + u_2^2 + u_3^2) + A_6 \xi_r^2 + A_7 \xi_v^2. \quad (49)$$

The temporal derivatives of macroscopic variables can be given according to the compatibility condition as

$$\int \left(\frac{\partial f^v}{\partial t} + u_i \frac{\partial f^v}{\partial x_i} \right) \boldsymbol{\psi}_v d\Xi_v = \mathbf{0}. \quad (50)$$

In a similar way, the above components $(A_1, \dots, A_6, A_7)^T$ in Eq.(48) can be determined uniquely.

References

- [1] Mars helicopter - nasa mars. <https://mars.nasa.gov/technology/helicopter/>, 2022.
- [2] Peter Atkins and Julio de Paula. Physical chemistry. eight ed, 2006.
- [3] EV Kustova and EA Nagnibeda. On a correct description of a multi-temperature dissociating co2 flow. *Chemical physics*, 321(3):293–310, 2006.
- [4] E Kustova, M Mekhonoshina, and A Kosareva. Relaxation processes in carbon dioxide. *Physics of Fluids*, 31(4):046104, 2019.
- [5] Raymond L Taylor and Steven Bitterman. Survey of vibrational relaxation data for processes important in the c o 2-n 2 laser system. *Reviews of Modern Physics*, 41(1):26, 1969.
- [6] RJ Stouffer, Syukuro Manabe, and K Bryan. Interhemispheric asymmetry in climate response to a gradual increase of atmospheric co2. *Nature*, 342(6250):660–662, 1989.
- [7] GRAHAM CANDLER. Computation of thermo-chemical nonequilibrium martian atmospheric entry flows. In *5th Joint Thermophysics and Heat Transfer Conference*, page 1695, 1990.
- [8] Y-K Chen, WD Henline, and ME Tauber. Mars pathfinder trajectory based heating and ablation calculations. *Journal of Spacecraft and Rockets*, 32(2):225–230, 1995.
- [9] Robert D Braun and Robert M Manning. Mars exploration entry, descent and landing challenges. In *2006 IEEE Aerospace Conference*, pages 18–pp. IEEE, 2006.
- [10] Elena Kustova and Mariia Mekhonoshina. Models for bulk viscosity in carbon dioxide. In *AIP Conference Proceedings*, volume 2132, page 150006. AIP Publishing LLC, 2019.
- [11] L Tisza. Supersonic absorption and stokes’ viscosity relation. *Physical Review*, 61(7-8):531, 1942.
- [12] Xingguo Pan, Mikhail N Shneider, and Richard B Miles. Power spectrum of coherent rayleigh-brillouin scattering in carbon dioxide. *Physical Review A*, 71(4):045801, 2005.
- [13] Mark S Cramer. Numerical estimates for the bulk viscosity of ideal gases. *Physics of fluids*, 24(6):066102, 2012.
- [14] Seyed Hossein Jamali, Mariette De Groen, Othonas A Moulτος, Remco Hartkamp, Thijs JH Vlugt, Wim Ubachs, and Willem Van De Water. Rayleigh-brillouin light scattering spectra of co2 from molecular dynamics. *The Journal of Chemical Physics*, 151(6):064201, 2019.
- [15] Yuanqing Wang, Wim Ubachs, and Willem Van De Water. Bulk viscosity of co2 from rayleigh-brillouin light scattering spectroscopy at 532 nm. *The Journal of Chemical Physics*, 150(15):154502, 2019.
- [16] Prabhu Lal Bhatnagar, Eugene P Gross, and Max Krook. A model for collision processes in gases. i. small amplitude processes in charged and neutral one-component systems. *Physical review*, 94(3):511, 1954.
- [17] Sydney Chapman and TG Cowling. The mathematical theory of non-uniform gases: An account of the kinetic theory of viscosity, thermal conduction and diffusion in gases. cambridge mathematical library. *Cambridge University Press*, 1:27–52, 1970.
- [18] Kun Xu. A gas-kinetic bgk scheme for the navier–stokes equations and its connection with artificial dissipation and godunov method. *Journal of Computational Physics*, 171(1):289–335, 2001.

- [19] Kun Xu. *Direct modeling for computational fluid dynamics: construction and application of unified gas-kinetic schemes*. World Scientific, 2015.
- [20] Jiequan Li and Zhifang Du. A two-stage fourth order time-accurate discretization for lax-wendroff type flow solvers i. hyperbolic conservation laws. *SIAM Journal on Scientific Computing*, 38(5):A3046–A3069, 2016.
- [21] Liang Pan, Kun Xu, Qibing Li, and Jiequan Li. An efficient and accurate two-stage fourth-order gas-kinetic scheme for the euler and navier-stokes equations. *Journal of Computational Physics*, 326:197–221, 2016.
- [22] Song Fu and Qibing Li. Numerical simulation of compressible mixing layers. *International journal of heat and fluid flow*, 27(5):895–901, 2006.
- [23] Wei Liao, Yan Peng, and Li-Shi Luo. Gas-kinetic schemes for direct numerical simulations of compressible homogeneous turbulence. *Physical Review E*, 80(4):046702, 2009.
- [24] G Kumar, Sharath S Girimaji, and J Kerimo. Weno-enhanced gas-kinetic scheme for direct simulations of compressible transition and turbulence. *Journal of Computational Physics*, 234:499–523, 2013.
- [25] Guiyu Cao, Liang Pan, and Kun Xu. Three dimensional high-order gas-kinetic scheme for supersonic isotropic turbulence i: criterion for direct numerical simulation. *Computers & Fluids*, 192:104273, 2019.
- [26] Guiyu Cao, Liang Pan, and Kun Xu. Three dimensional high-order gas-kinetic scheme for supersonic isotropic turbulence ii: Coarse-graining analysis of compressible ksgs budget. *Journal of Computational Physics*, 439:110402, 2021.
- [27] Guiyu Cao, Kun Xu, Liang Pan, and Shiyi Chen. High-order gas-kinetic scheme in general curvilinear coordinate for iles of compressible wall-bounded turbulent flows. *arXiv preprint arXiv:2107.08609*, 2021.
- [28] Guiyu Cao, Liang Pan, and Kun Xu. High-order gas-kinetic scheme with parallel computation for direct numerical simulation of turbulent flows. *Journal of Computational Physics*, 448:110739, 2022.
- [29] Kun Xu and Juan-Chen Huang. A unified gas-kinetic scheme for continuum and rarefied flows. *Journal of Computational Physics*, 229(20):7747–7764, 2010.
- [30] Juan-Chen Huang, Kun Xu, and Pubing Yu. A unified gas-kinetic scheme for continuum and rarefied flows iii: Microflow simulations. *Communications in Computational Physics*, 14(5):1147–1173, 2013.
- [31] Yajun Zhu, Chang Liu, Chengwen Zhong, and Kun Xu. Unified gas-kinetic wave-particle methods. ii. multiscale simulation on unstructured mesh. *Physics of Fluids*, 31(6):067105, 2019.
- [32] Chang Liu, Yajun Zhu, and Kun Xu. Unified gas-kinetic wave-particle methods i: Continuum and rarefied gas flow. *Journal of Computational Physics*, 401:108977, 2020.
- [33] Xiaojian Yang, Wei Shyy, and Kun Xu. Unified gas-kinetic wave-particle method for gas-particle two-phase flow from dilute to dense solid particle limit. *Physics of Fluids*, 34(2):023312, 2022.
- [34] Chunpei Cai, Danny D Liu, and Kun Xu. One-dimensional multiple-temperature gas-kinetic bhatnagar-gross-krook scheme for shock wave computation. *AIAA journal*, 46(5):1054–1062, 2008.
- [35] Guiyu Cao, Hualin Liu, and Kun Xu. Physical modeling and numerical studies of three-dimensional non-equilibrium multi-temperature flows. *Physics of Fluids*, 30(12):126104, 2018.
- [36] Hualin Liu, Guiyu Cao, and Weifang Chen. Multiple-temperature gas-kinetic scheme for type iv shock/shock interaction. *Communication in Computational Physics*, page 853, 2021.
- [37] Marcos Castro, Bruno Costa, and Wai Sun Don. High order weighted essentially non-oscillatory weno-z schemes for hyperbolic conservation laws. *Journal of Computational Physics*, 230(5):1766–1792, 2011.
- [38] Gary N Coleman, John Kim, and Robert D Moser. A numerical study of turbulent supersonic isothermal-wall channel flow. *Journal of Fluid Mechanics*, 305:159–183, 1995.
- [39] Peng Zhang and Zhenhua Xia. Contribution of viscous stress work to wall heat flux in compressible turbulent channel flows. *Physical Review E*, 102(4):043107, 2020.
- [40] XiaoPing Chen, XinLiang Li, and ZuChao Zhu. Effects of dimensional wall temperature on velocity-temperature correlations in supersonic turbulent channel flow of thermally perfect gas. *SCIENCE CHINA Physics, Mechanics & Astronomy*, 62(6):1–11, 2019.
- [41] John David Anderson. *Hypersonic and high temperature gas dynamics*. Aiaa, 2000.
- [42] Frank M White and Joseph Majdalani. *Viscous fluid flow*, volume 3. McGraw-Hill New York, 2006.

- [43] George Emanuel. Bulk viscosity of a dilute polyatomic gas. *Physics of Fluids A: Fluid Dynamics*, 2(12):2252–2254, 1990.
- [44] JG Parker. Rotational and vibrational relaxation in diatomic gases. *The Physics of Fluids*, 2(4):449–462, 1959.
- [45] E Kustova, I Alekseev, and L Tan. Investigation of shock wave structure in co2 based on the continuum and dsmc approaches. In *Journal of Physics: Conference Series*, volume 1959, page 012032. IOP Publishing, 2021.
- [46] Zhao Wang, Hong Yan, Qibing Li, and Kun Xu. Unified gas-kinetic scheme for diatomic molecular flow with translational, rotational, and vibrational modes. *Journal of Computational Physics*, 350:237–259, 2017.
- [47] TF Morse. Kinetic model for gases with internal degrees of freedom. *The physics of fluids*, 7(2):159–169, 1964.
- [48] Henning Struchtrup. The bgk model for an ideal gas with an internal degree of freedom. *Transport theory and statistical physics*, 28(4):369–385, 1999.
- [49] Guiyu Cao. *High-order gas-kinetic schemes for turbulence modeling and simulation*. Hong Kong University of Science and Technology (Hong Kong), 2021.
- [50] Eleuterio F Toro. *Riemann solvers and numerical methods for fluid dynamics: a practical introduction*. Springer Science & Business Media, 2013.
- [51] Ming Yu, Chun-Xiao Xu, and Sergio Pirozzoli. Genuine compressibility effects in wall-bounded turbulence. *Physical Review Fluids*, 4(12):123402, 2019.
- [52] PG Huang and Gary N Coleman. Van driest transformation and compressible wall-bounded flows. *AIAA journal*, 32(10):2110–2113, 1994.
- [53] Kenneth J Franko and Sanjiva K Lele. Breakdown mechanisms and heat transfer overshoot in hypersonic zero pressure gradient boundary layers. *Journal of Fluid Mechanics*, 730:491–532, 2013.
- [54] Yipei Chen, Yajun Zhu, and Kun Xu. A three-dimensional unified gas-kinetic wave-particle solver for flow computation in all regimes. *Physics of Fluids*, 32(9):096108, 2020.